

Dynamic monitoring of flood disaster based on remote sensing data cube

Zhicheng Wang (✉ zawang@yic.ac.cn)

Yantai Institute of Coastal Zone Research <https://orcid.org/0000-0003-4033-4067>

Zhiqiang Gao

Yantai Institute of Coastal Zone Research

Research Article

Keywords: Flood disaster, Data cube, Remote sensing, spatio-temporal data fusion algorithm

Posted Date: March 17th, 2022

DOI: <https://doi.org/10.21203/rs.3.rs-1442170/v1>

License:   This work is licensed under a Creative Commons Attribution 4.0 International License.

[Read Full License](#)

Dynamic monitoring of flood disaster based on remote sensing data cube

Zhicheng Wang^{1,2,3} Zhiqiang Gao^{2,3}

Abstract

High-frequency dynamic monitoring of flood disaster using remote sensing technology is crucial for accurate decision-making of disaster prevention and relief. However, the current trade-off between spatial and temporal resolution of remote sensing sensors limits their application in high-frequency dynamic monitoring of flood disaster. To deal with this challenge, in this study, first, to construct the cloud-free MODIS data cube, we removed the cloudy areas in MODIS original data cube by using the information provided by GPM rainfall data. Then, we fused the cloud-free MODIS data cube and Landsat-8 data by using the spatio-temporal data fusion algorithm to construct the high spatio-temporal resolution (Landsat-like) data cube. Last, the high spatio-temporal resolution (Landsat-like) data cube was used for high-frequency dynamic monitoring of flood disaster. Our study had three main results: (1) The differences between cloud-free MODIS data cube and observations were small and the cloud-free MODIS data cube could be used for subsequent studies. (2) High spatio-temporal resolution (Landsat-like) data cube reflected the spatio-temporal changes of flood well and could be used for the high-frequency dynamic monitoring of flood disaster. (3) There were two floods occurred in the study area from July 17, 2021 to October 16, 2021. The first flood occurred from July 17, 2021 to September 15, 2021, with maximum affected area of 668.36 km². The second flood occurred from September 18, 2021 to October 16, 2021, with maximum affected area of 303.88 km². Our study provides a general method for high-frequency monitoring of flood disaster.

Keywords Flood disaster Data cube Remote sensing spatio-temporal data fusion algorithm

1 Introduction

Flood disaster is one of the most common and destructive disasters in the natural world (Khan et al., 2011), which can have a serious impact on the ecological environment, agriculture and economy of the flood-affected region (Chen et al., 2012 ; Gianinetto et al., 2006). Timely and accurate monitoring of flood disaster is essential for rapid response, effective decision-making, and disaster mitigation (Chen et al., 2018). Due to the large inundated area, it is tough to monitor the flood disaster by traditional ground survey methods (Dao and Liou, 2015 ; Sanyal and Lu, 2004). Therefore, an effective monitoring method is in need to conduct the dynamic monitoring of flood disaster.

In recent years, remote sensing technology has played a huge role in disasters monitoring, because it can achieve simultaneous monitoring of large area and this technology is economical (Zhang et al., 2014). Generally, there are two kinds of remote sensing technologies to monitor flood disaster, including active remote sensing and passive remote sensing. Active remote sensing realizes flood disaster monitoring by transmitting microwave to flood and receiving backscatter signal. Among most of the active remote sensing sensors, Sentinel-1 (Tsyganskaya et al., 2018 ; Mehrabi, 2021) and TerraSAR (Cruz et al., 2010 ; Voormansik et al., 2014) are widely used in flood disaster monitoring. Active remote sensing can work in cloudy weather because of the ability of microwave's penetrating clouds and water vapor

✉ Zhiqiang Gao
zqgao@yic.ac.cn

39 (Henry et al., 2003 ; Henry et al., 2006 ; Mallinis et al., 2013), which makes active remote sensing more
40 efficient for flood disaster monitoring during rainy days (Pulvirenti et al., 2011). Nonetheless, due to the
41 low spatial and temporal resolution of active remote sensing sensors, active remote sensing data cannot
42 always be obtained during the flood period, and it is impossible to realize the high-frequency dynamic
43 monitoring of flood disaster by active remote sensing.

44 Compared to active remote sensing, passive remote sensing conducts flood disaster monitoring by
45 using visible bands emitted by the sun; and it has great potential in flood disaster monitoring because of
46 higher spatial and temporal resolution, abundant band information and low cost. Over the past years,
47 Landsat series data (Diaz-Delgado et al., 2016 ; Olthof, 2017), MODIS data (Fuentes et al., 2019 ; Hu et
48 al., 2021) and Sentinel-2 (Guo et al., 2021 ; Zhang et al., 2021) data have arisen great attention in
49 monitoring flood disaster. However, it is impossible for passive remote sensing to obtain images with
50 both high spatial and high temporal resolution due to the limitation of current technology. For example,
51 Landsat provides images with a spatial resolution of 30 m, but its temporal resolution is 16 days, which
52 makes it impossible to conduct intensive dynamic monitoring of flood disaster; in contrast, MODIS
53 images' temporal resolution is 1 day and its spatial resolution is 250-1000 m (Wang et al., 2020), which
54 makes it hard to capture fine flood disaster information. The tradeoff between spatial and temporal
55 resolution has become a barrier for application of passive remote sensing in high-frequency flood disaster
56 monitoring.

57 In order to deal with the challenge that high spatial and high temporal resolution cannot be taken
58 into account at the same time, scholars have proposed spatio-temporal data fusion algorithms to generate
59 remote sensing images with both high spatial and high temporal resolution by fusing low temporal
60 resolution but high spatial resolution images with low spatial resolution but high temporal resolution
61 images (Chen et al., 2015). Images with both high spatial and high temporal resolution make up high
62 spatial-temporal resolution image data cube in time dimension. Therefore, it is possible to perform high-
63 frequency dynamic monitoring of flood disaster using the high spatial-temporal resolution image data
64 cube generated by the spatio-temporal data fusion algorithms. Many spatio-temporal data fusion
65 algorithms have been proposed, including STARFM (Gao et al., 2006), ESTARFM (Zhu et al., 2010),
66 FSDAF (Zhu et al., 2016) and so on. The input data of these algorithms are: (a) high spatial resolution,
67 low temporal resolution image at t_0 (b) high temporal resolution, low spatial resolution image at t_0 and
68 (c) high temporal resolution, low spatial resolution image at t_1 . And the output data is image with both
69 high spatial and high temporal resolution. Up to now, the spatio-temporal data fusion algorithms have
70 been successfully applied to land use change monitoring (Liu et al., 2021), vegetation phenology
71 monitoring (Shen et al., 2021), urban heat island effect monitoring (Shen et al., 2016); although these
72 applications may be affected by clouds, the cloud-free pixel information can be used by traditional cloud
73 removal algorithms such as NSPI (Chen et al., 2011), SAMSTS (Yan and Roy, 2018) to achieve the goal
74 of cloud removal. Since the traditional cloud removal algorithms have poor effect on images containing
75 emergency events such as flood disaster, it is not suitable for the monitoring of flood disaster. Therefore,
76 it is necessary to employ other data to remove the cloud areas in the field of flood disaster monitoring.

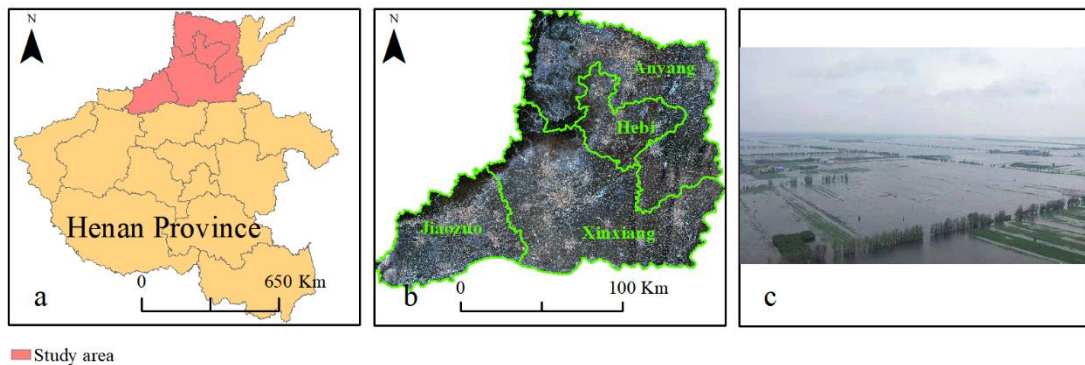
77 In this study, in order to overcome the shortcoming of the above-mentioned cloud removal
78 algorithms, we used GPM rainfall data to construct the weight factor, and removed cloud areas in MODIS
79 images by using the weight factor and information provided by cloud-free pixels, and finally the low
80 spatial but high temporal cloud-free MODIS data cube was generated; in order to resolve the difficulty
81 that monitoring of flood disaster by remote sensing technology cannot take into account both high spatial
82 and high temporal resolutions, we constructed high spatial and temporal resolution remote sensing data

83 cube (Landsat-like data cube) by fusing cloud-free MODIS data cube and Landsat data based on spatio-
84 temporal data fusion algorithm to achieve high-frequency dynamic monitoring of flood disaster.

85 The main objectives of this study were: (1) to verify the feasibility of using GPM rainfall data to
86 remove cloud areas in MODIS images; (2) to use spatio-temporal data fusion algorithm to construct
87 Landsat-like data cube with both high spatial and high temporal resolution, and to verify the feasibility
88 of using the Landsat-like data cube for high-frequency flood disaster monitoring; and (3) to perform
89 high-frequency dynamic monitoring of flood disaster in Anyang City, Hebi City, Jiaozuo City and
90 Xinxiang City in Henan Province based on Landsat-like data cube.

91 2 Study area

92 We selected Anyang City, Hebi City, Jiaozuo City, and Xinxiang City in Henan Province, China as our
93 study area which is located in the north of Henan Province (Fig. 1) and has the total area of 21759.7 km².
94 Main land use types of study area are cultivated land, forest land, construction land, and water bodies.
95 The climate in study area is the temperate continental monsoon climate. From July 17, 2021 to July 30,
96 2021, under the influence of typhoon "Yanhua", a heavy rainstorm occurred in the study area and caused
97 flood disaster in the study area. In September 2021, there was a second flood disaster due to consecutive
98 rainy days. Two flood disasters had a huge side impact on ecological environment and production
99 activities in the study area.



101 **Fig. 1** a: the location of study area in Henan Province, b: Landsat-8 OLI image of study area, c: flood
102 photo taken in study area

103 3 Data and methods

104 3.1 Data

105 As shown in Table 1, seven kinds of data were used. Some of the Landsat-8 data and MODIS daily
106 reflectance data (MOD09GA) were used as input data of spatio-temporal data fusion algorithm to
107 generate high spatial and temporal resolution Landsat-like data cube; GPM rainfall data were used to
108 construct weights for removal of cloud areas in MODIS data; Sentinel-1 data, Sentinel-2 data, some of
109 the Landsat-8 data, GF-1 data and GF-3 data were used to evaluate the accuracy of the extracted flood-
110 inundated area.

111 3.2 Methods

112 3.2.1 Constructing cloud-free MODIS data cube

113 There are data-missing areas in MODIS images due to the influence of clouds. In this study, cloud areas
 114 in MODIS images were removed using the “Fill-Fit” method proposed by (Yan and Roy, 2020). Different
 115 from “Fill” step in “Fill-Fit” method which uses similar pixels to fill the data-missing areas, our “Fill”
 116 step constructs weighting factors by using GPM rainfall data and then makes use of the information
 117 provided by the valid pixels before and after the data-missing areas to fill the data-missing areas.

118 The pixel value in the remote sensing image is the reflectance value of a ground object
 119 corresponding to the pixel at a certain wavelength. As described in (Liu et al., 2002), with the increase
 120 of the water content of a ground object, the reflectance value of this ground object will decrease for all
 121 the wavelengths. Therefore, we propose that the rainfall increases the water content of the ground objects,
 122 which reduces the reflectance values of the ground objects, and the more rainfall, the faster the
 123 reflectance values of the ground objects decrease; when there is flood on the ground, the reflectance
 124 values will be close to that of the flood water. In addition, we suppose that the reflectance values of
 125 ground objects change linearly during a short time period. For a pixel, its time series are:

$$[r_m, r_n, r_{n+1}, r_{n+2}, r_k] \quad (1)$$

127 where r_n, r_{n+1} and r_{n+2} are the reflectance values at time t_n, t_{n+1} and t_{n+2} respectively, and these
 128 values are missing because of the influence of clouds; r_m and r_k are the reflectance values at time t_m
 129 and t_k respectively, these values are valid. Furthermore, the rainfall of this pixel at time t_n, t_{n+1} and
 130 t_{n+2} are p_n, p_{n+1} and p_{n+2} respectively. Then, r_n can be calculated by the following equation:

$$r_n = r_m + (r_k - r_m) \times w \quad (2)$$

$$w = \frac{p_n}{p_n + p_{n+1} + p_{n+2}} \quad (3)$$

133 After the above equations were used to fill all the pixels of missing data, the time series reflectance
 134 values of each pixel were fitted by linear harmonic model. The fitted results constituted a cloud-free data
 135 cube with low spatial and high temporal resolution in time dimension.

136 **Table 1** Data used in this study

Data	Spatial resolution	Time range	Usage
Landsat-8	30 m	2020.5.22	Input of spatio-temporal data fusion algorithm
		2021.9.30, 2021.10.16	Evaluating the extracted flood results
MODIS	500 m	2020.5.22	Input of spatio-temporal data fusion algorithm
		2021.7.17-2021.10.17	Constructing cloud-free MODIS data cube
GPM rainfall data	0.1°	2021.7.17-2021.10.17	Constructing weights to remove clouds in MODIS data
GF-3	10 m	2021.7.24	Evaluating the extracted flood results
Sentinel-1	5 m×20 m	2021.7.17-2021.10.17	
Sentinel-2	10 m, 20 m, 60 m		
GF-1	16 m		

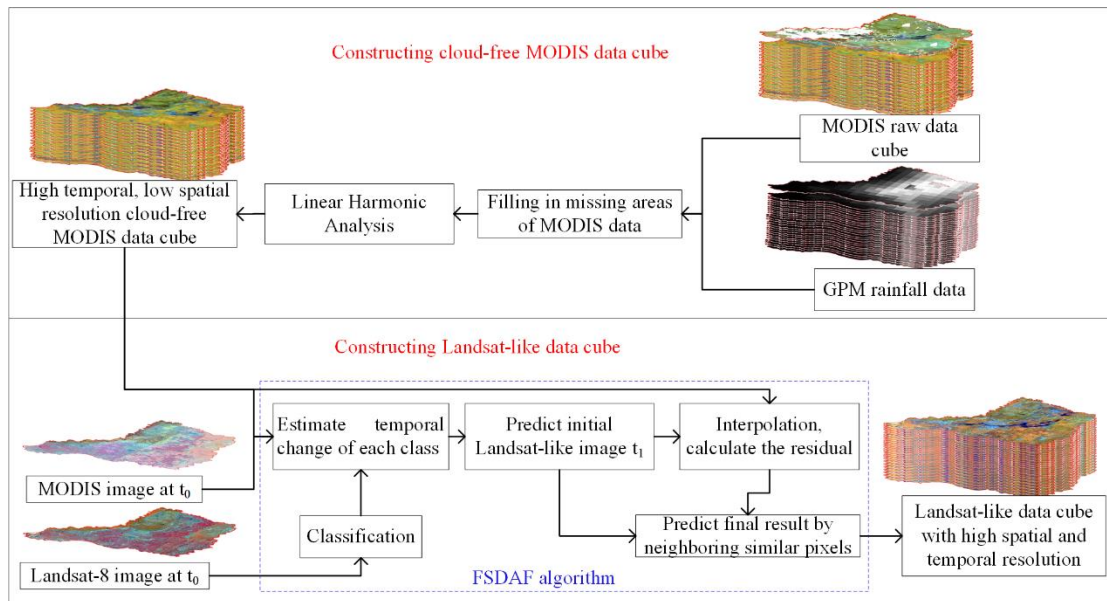
137

138 3.2.2 Constructing Landsat-like data cube

139 We used spatio-temporal data fusion algorithm to construct Landsat-like data cube. Among all spatio-

140 temporal data fusion algorithms. We selected the FSDAF algorithm which can predict land use changes
 141 well. As shown in Fig. 2, the input data of FSDAF algorithm are: Landsat-8 OLI image and MODIS
 142 image at t_0 , another MODIS image at t_1 ; the output of FSDAF algorithm is Landsat-like image with both
 143 high spatial and high temporal resolution which constitutes the Landsat-like data cube in time dimension.
 144 It should be pointed out that, when running the FSDAF algorithm, a MODIS image at t_1 is taken from
 145 the cloud-free MODIS data cube.

146 FSDAF algorithm includes five main steps: (1) Classify Landsat-8 OLI image at t_0 , and calculate
 147 the proportion of each class in each pixel of MODIS image at t_0 . (2) Estimate temporal change of each
 148 class. (3) Predict initial Landsat-like image t_1 . (4) Interpolate the MODIS image at t_1 by using thin plate
 149 spline method, and calculate the residual of each band. (5) Predict the final result by using neighboring
 150 similar pixels.



151

152 **Fig. 2** Flow chart of constructing cloud-free MODIS data cube and Landsat-like data cube

152

153 3.2.3 Extracting flooded area

154 By using the random forest algorithm, we extracted the flooded area from Landsat-like data cube. Since
 155 the generated flood spatial distribution didn't change obviously in the adjacent time, we took out the
 156 extracted results at a certain interval as our final results.

157 3.2.4 Evaluating cloud-free MODIS data cube

158 We evaluated the cloud-free MODIS data cube from quantitative and qualitative aspects. In quantitative
 159 evaluation, we simulated the cloud areas using observed data and used the method in section 3.2.1 to
 160 remove the simulated cloud areas; then we calculated root mean square error (RMSE), mean difference
 161 (MEAN_DIFF) and correlation coefficient (R) between observed data and the results of cloud removal.
 162 In qualitative evaluation, we visually compared the images with cloud areas with their corresponding
 163 results after cloud removed.

164 3.2.5 Evaluating Landsat-like data cube

165 Evaluations are usually performed by comparing Landsat-like images in Landsat-like data cube with its
 166 corresponding Landsat images. However, most Landsat images in the period of this study were covered

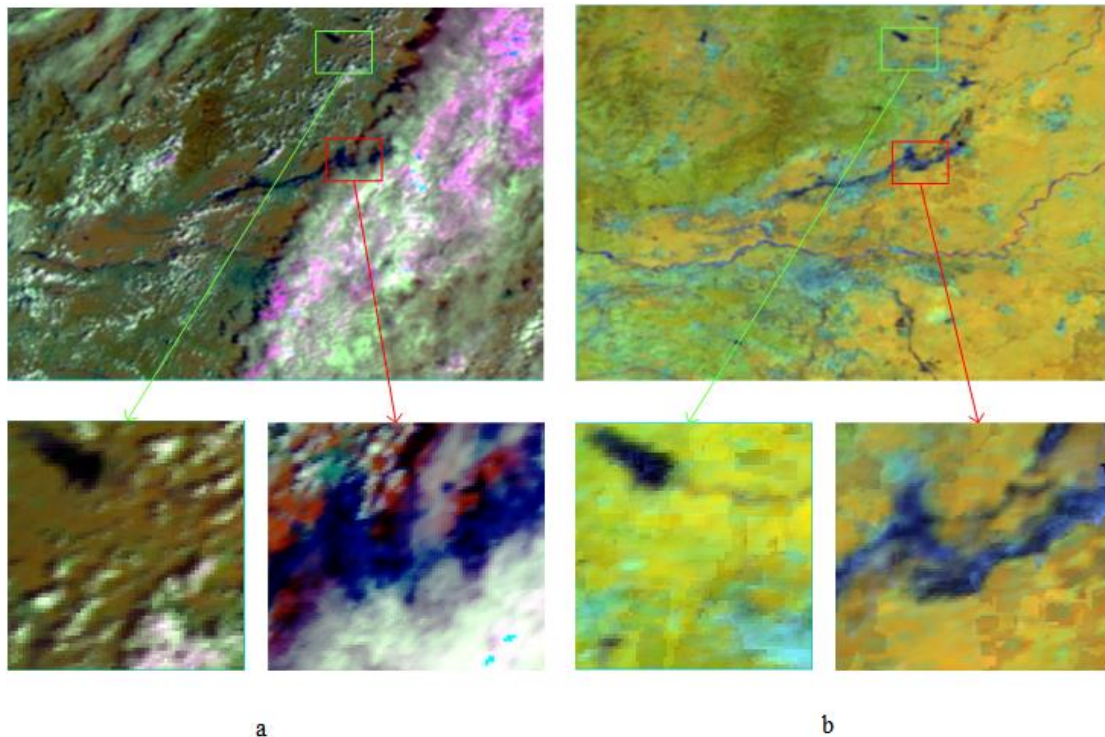
167 by cloud areas and couldn't be used. Therefore, we evaluated Landsat-like data cube from three aspects:
168 (1) visually evaluated the Landsat-like data cube; (2) evaluated the accuracy of flood extraction results,
169 which could indirectly reflect the quality of Landsat-like cube; (3) Compared flood results extracted from
170 reference data with that from Landsat-like data cube.

171 3.2.6 Evaluating the accuracy of flood extraction results

172 Due to the small number of available reference images, it was impossible to evaluate the accuracy
173 of each flood extraction result by using the corresponding reference image of the same date. We
174 adopted a compromise scheme, that was, using reference images closed to the date of flood
175 extraction results to evaluate the accuracy. After evaluation, flood extraction results were compared
176 with each other and adjusted manually, and finally reliable flood extraction results were obtained.

177 4 Results

178 4.1 Evaluation results of cloud-free MODIS data cube



179
180 **Fig. 3** Comparison between original MODIS image and image in cloud-free MODIS data cube. a:
181 original MODIS image. b: image in cloud-free MODIS data cube (Images are in pseudo color
182 composition for display, Band2-Red, Band6-Green, Band1-Blue)

183 Table 2 shows the RMSE, MEAN_DIFF and R at different wavelengths. First, the RMSE and
184 MEAN_DIFF at short wavelengths (band3, band4, and band1) were lower than those at long wavelengths
185 (band2, band6, and band7), and they were lower than 0.007 and 0.003 respectively, which indicated that
186 the method in section 3.2.1.1 can achieve better results at short wavelengths. Second, MEAN_DIFF
187 values at short (band3, BAND4 and BAND1) and long wavelengths (band2, band6 and band7) were
188 lower and higher than 0 respectively, indicating that reflectance values after cloud removal were lower

189 than the original reflectance values at short wavelengths and higher than the original reflectance values
 190 at long wavelengths. Therefore, the flood area extracted from images at short wavelengths would be
 191 larger than that from images at long wavelengths. Third, the correlation coefficient R at band3 and band4
 192 were 0.75 and 0.71 respectively, which might be caused by high variances of band3 and band4; while the
 193 correlation coefficients at other bands were all higher than 0.85, indicating that there was a strong linear
 194 correlation between reflectance values after cloud removal and the reflectance values. As can be seen
 195 from Fig. 3, thin cloud and thick cloud were well removed using method in section 3.2.1, and flood
 196 information were well retained in the generated cloud-free MODIS image.

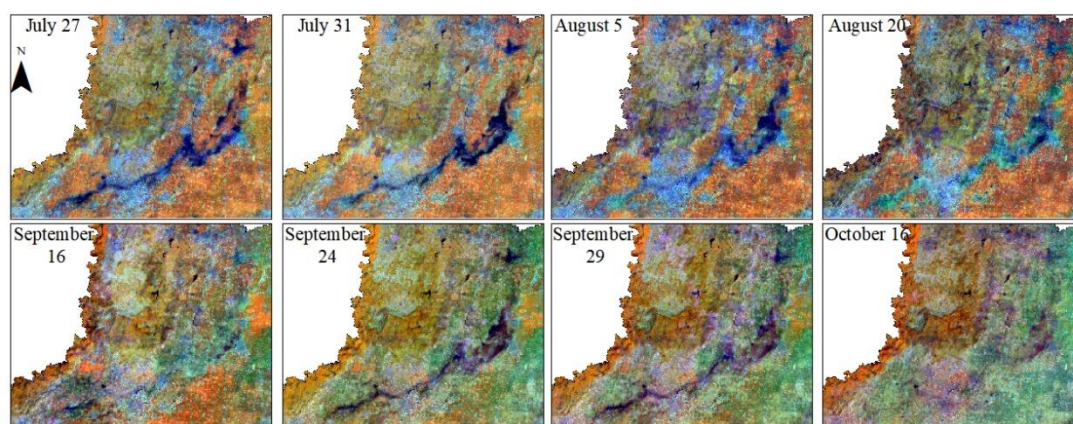
197 In general, using method in section 3.2.1 to generate low spatial, high temporal resolution cloud-
 198 free MODIS data cube could achieve a good effect, and the results could be used for subsequent studies.

199 **Table 2** Evaluation results of cloud-free MODIS data cube

Band	RMSE	MEAN_DIFF	R
band1	0.0061	-0.0009	0.89
Band2	0.0143	0.0061	0.94
Band3	0.0068	-0.0017	0.75
Band4	0.0093	-0.0024	0.71
Band6	0.0117	0.0057	0.86
Band7	0.0074	0.0033	0.93

200

201 4.2 Evaluation results of Landsat-like data cube



202

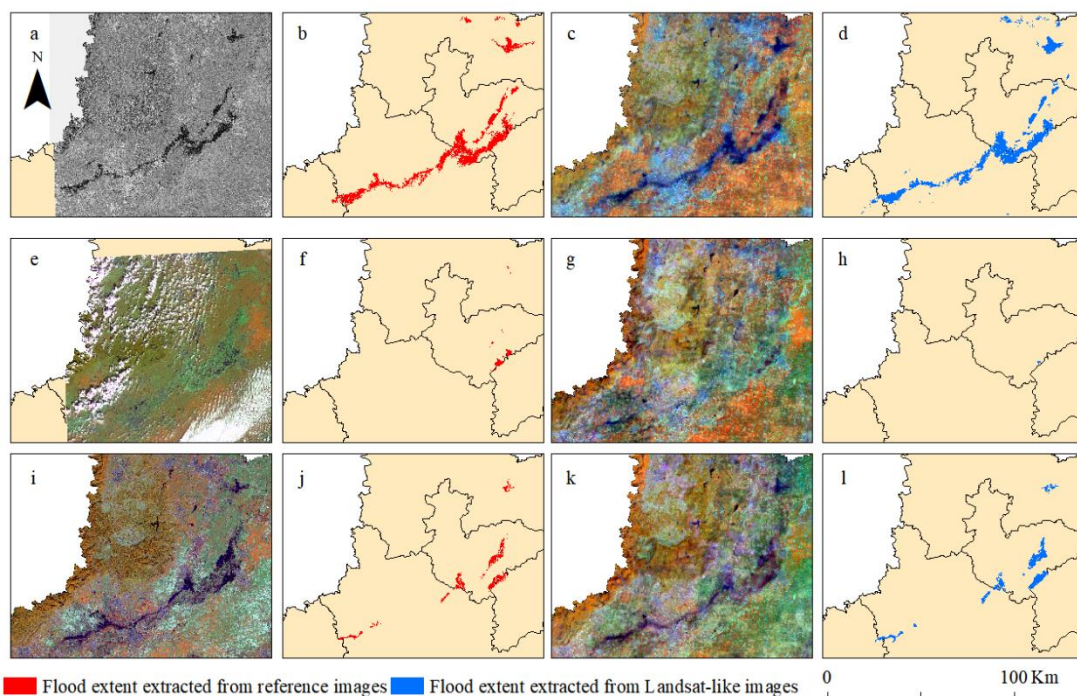
203 **Fig. 4** Randomly selected Landsat-like images. (Images are in pseudo color composition for display,
 204 Band2-Red, Band6-Green, Band1-Blue)

205 The spatial resolution of both observed Landsat images and images in Landsat-like data cube generated
 206 by the spatiotemporal data fusion algorithm was 30 m. However, the temporal resolution of observed
 207 Landsat images was 16 days, relatively low; and there were large areas of missing data in images because
 208 of the influence of clouds, which resulted in discontinuous spatial coverage. Therefore, it was impossible
 209 to capture the dynamic changes of flood disasters by observed Landsat images in detail. On the contrary,
 210 the temporal resolution of Landsat-like data cube could reach 1 day, and the effects of clouds were
 211 eliminated. High-frequency dynamic monitoring of flood disasters could be achieved by using Landsat-
 212 like data cube.

213 We randomly selected eight Landsat-like images between July 17, 2021 and October 17, 2021 for

214 display (Fig. 4). In general, Landsat-like data cube generated by the spatio-temporal data fusion algorithm
 215 were effective. Its spatial coverage was complete and continuous, and it reflected the spatial distributions
 216 of each land use type (such as vegetation, construction land, water body, cultivated land, etc.). The extent
 217 of flood disasters in each image was clearly visible. However, some noises appeared in Landsat-like
 218 images, which was mainly caused by cloud shadows in some MODIS images; and it didn't affect the
 219 high-frequency dynamic monitoring of floods using Landsat-like data cubes.

220 In terms of the accuracy evaluation of flood extraction results, most of the overall accuracy,
 221 producer accuracy and user accuracy were higher than 0.80, indicating that the flood extraction results
 222 were good. The flood extraction result on July 31 was the best, and its overall accuracy, producer
 223 accuracy and user accuracy were the highest. In addition, its Kappa coefficient was 0.83, indicating that
 224 the reference data had a good consistency with the extraction result. This was mainly because the weather
 225 on July 31 was clear, and MODIS image had no data missing areas, which made the generated Landsat-
 226 like image on July 31 closed to the real image. But there was an undesired evaluation results on July 24,
 227 the overall accuracy, producer accuracy and user accuracy were 0.78, 0.79 and 0.76 respectively, and its
 228 Kappa coefficient was 0.73, which mainly due to the compromise evaluation scheme of flood extraction
 229 results we adopted and the small number of reference images before July 24.



230
 231 **Fig. 5** Comparison of the flood extent extracted from the reference images and from the Landsat-like
 232 images. a, e and i are reference images, corresponding to Sentinel-1 image on July 27, Sentinel-2 image
 233 on September 14, and Landsat-8 image on September 30 respectively; b, f, and j are flood extents
 234 extracted from reference images; c, j, and k are Landsat-like images corresponding to reference images;
 235 d, h and l are flood extents extracted from Landsat-like images. (Images are in pseudo color composition
 236 for display, Band2-Red, Band6-Green, Band1-Blue)

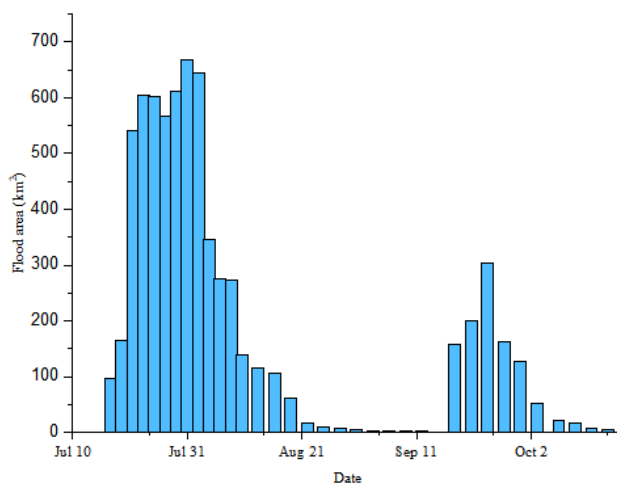
237 Fig. 5 shows the comparisons between reference images and Landsat-like images. In general, the
 238 flood extents from the three kinds of reference images are consistent with those from the Landsat-like
 239 images on the corresponding date. Among them, flood extraction results from reference images on July
 240 27 and September 30 have the best consistency with those from the corresponding Landsat-like images,

241 while there was a slight difference on September 14 between flood extraction results from reference
242 image and Landsat-like image.

243 Above analyses verify the quality of Landsat-like data cube generated by spatio-temporal data
244 fusion algorithm and the accuracy of flood extraction results.

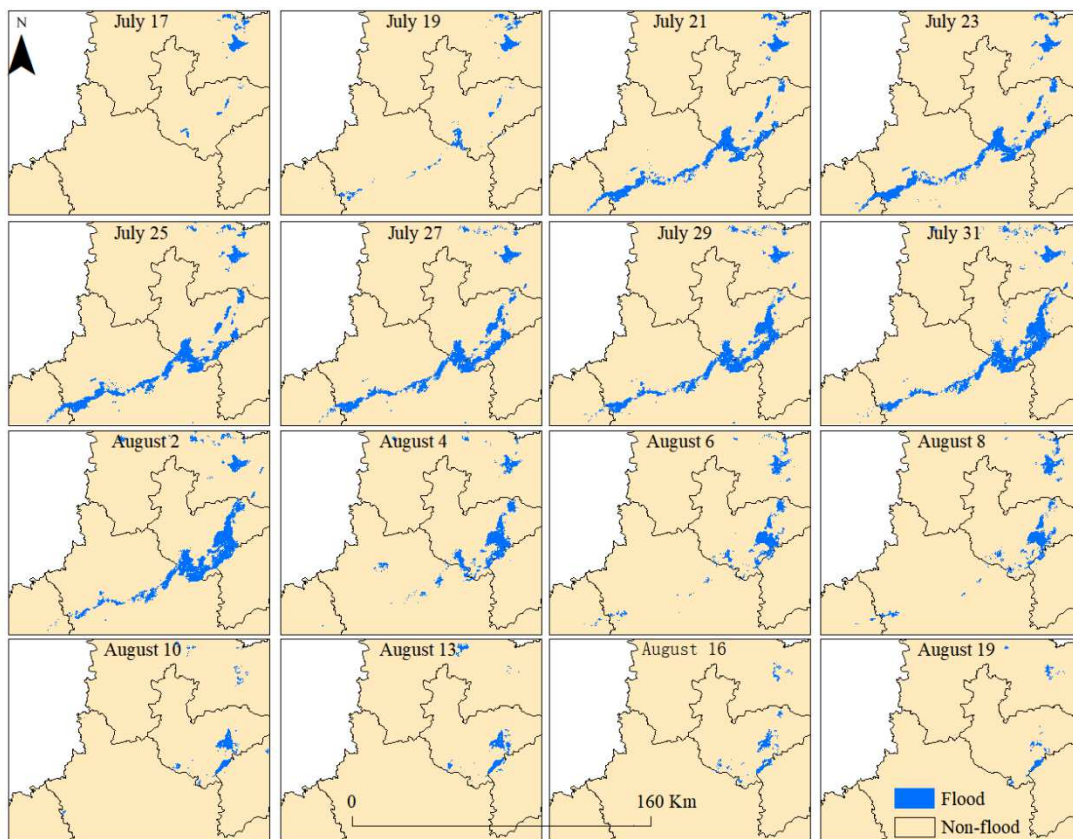
245 4.3 Flood disaster monitoring results based on Landsat-like data cube

246 Fig. 6 and Fig. 7-9 show the statistics of flood areas and the spatial distribution of flood disaster
247 respectively. High-frequency monitoring of flood disaster could be achieved very well by Landsat-like
248 data cube.



249

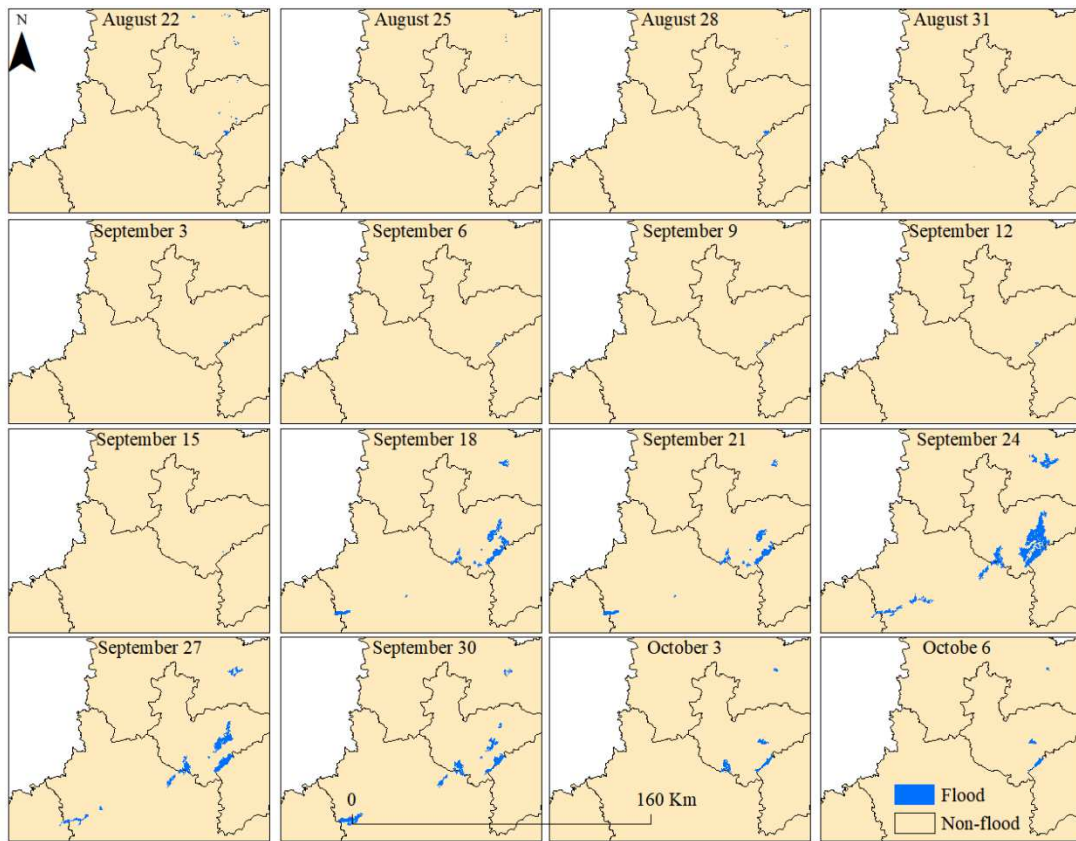
250 **Fig. 6** Flood areas



251

252 **Fig. 7** Flood extents during July 17 to August 19

253 There are two peaks in Fig. 6, indicating that the study area experienced two flood disasters from
 254 July 17 to October 16 and the first was more severe than the second. The first flood disaster was during
 255 July 17 to September 15. The growth period and the recession period of the first flood disaster were July
 256 17 to July 31 and July 31 to September 15 respectively. The area increased from 95.53 km² to 668.36
 257 km² and the spatial distribution gradually expanded from north to south, from scattered point distribution
 258 to concentrated plane distribution in the growth period; while in the recession period, the flood area
 259 decreased from the maximum value of 668.36 km² to 0.56 km², and the spatial distribution gradually
 260 shrank from south to north and from outside to inside until August 22 when the flood distribution turned
 261 into point-like distribution. The second flood disaster occurred from September 15 to October 16. During
 262 the growth period from September 15 to September 24, the flood area increased from 0.56 km² to 303.88
 263 km², with the spatial distribution reaching the widest range on September 24; while in the recession
 264 period from September 24 to October 16, the flood area decreased to 3.95 km², and the spatial distribution
 265 shrank from west to east.



266

267 **Fig. 8** Flood extents during August 22 to October 6



268

269

Fig. 9 Flood extents during October 9 to October 15

270

271 **5 Conclusions**

272 In this study, GPM rainfall data was introduced to remove clouds in MODIS images, which overcame
273 the shortcoming of traditional cloud removal methods. Landsat-like data cube with high spatio-temporal
274 resolution were constructed based on spatio-temporal data fusion algorithm, which resolved the difficulty
275 that flood monitoring by traditional remote sensing technology could not take into account both high
276 spatial resolution and high temporal resolution. Finally, high-frequency dynamic monitoring of flood
277 disasters was realized based on Landsat-like data cube with high spatial and temporal resolution. The
278 following conclusions were drawn:

279 (1) Images in low spatial, high temporal resolution cloud-free MODIS data cube generated by using
280 method in section 3.2.1.1 were less different from their corresponding real data, and they could be used
281 as the input of spatio-temporal data fusion algorithm to generate high spatio-temporal resolution Landsat-
282 like data cube.

283 (2) Landsat-like data cube generated by spatio-temporal data fusion algorithm had both high spatial
284 resolution and high temporal resolution; spatial coverage was complete and continuous; temporal
285 coverage was dense. Furthermore, Landsat-like data cube reflected the spatio-temporal changes of flood
286 disasters well. Therefore, Landsat-like data cube could achieve high-frequency dynamic monitoring of
287 flood disasters.

288 (3) The flood disaster monitoring results based on high spatial and temporal resolution Landsat-like
289 data cube generated by spatio-temporal data fusion algorithm showed that two flood disasters occurred
290 in the study area from July 17 to October 16. The first was during July 17 to September 15 with maximum
291 affected area of 668.36 km². The second was from September 15 to October 16 with maximum affected
292 area of 303.88 km².

293 **Author contributions** All authors have made a substantial contribution to this research and have
294 approved the final manuscript. Zhicheng Wang contributed to data processing, writing; and Zhiqiang Gao
295 contributed to data acquiring, checking results of data processing and checking manuscript.

296 **Funding** This work was supported from NSFC fund project (41876107), Key Research Program of
297 Frontier Science, Chinese Academy of Sciences (ZDBS-LY-7010), the Open Fund of CAS Key
298 Laboratory of Marine Ecology and Environmental Sciences (KLMEES202005).

299 **Declarations**

300 **Conflict of interest** None.

301

302

303

304

305

306

307

308

309 **References**

- 310 Chen B, Huang B, Xu B 2015. Comparison of Spatiotemporal Fusion Models: A Review. Remote
311 Sensing [J], 7: 1798-1835. <https://doi.org/10.3390/rs70201798>
- 312 Chen J, Zhu X L, Vogelmann J E, et al. 2011. A simple and effective method for filling gaps in Landsat
313 ETM plus SLC-off images. Remote Sensing of Environment [J], 115: 1053-1064.
314 <https://doi.org/10.1016/j.rse.2010.12.010>
- 315 Chen Y Z, Syvitski J P M, Gao S, et al. 2012. Socio-economic Impacts on Flooding: A 4000-Year History
316 of the Yellow River, China. Ambio [J], 41: 682-698. [https://doi.org/10.1007/s13280-012-0290-](https://doi.org/10.1007/s13280-012-0290-5)
317 [5](https://doi.org/10.1007/s13280-012-0290-5)
- 318 Chen Z Q, Chen N C, Du W Y, et al. 2018. An active monitoring method for flood events. Computers &
319 Geosciences [J], 116: 42-52. <https://doi.org/10.1016/j.cageo.2018.04.009>
- 320 Cruz V H, Muller M, Weise C 2010. Flood Extent Mapping Based on TerraSAR-X Data.
321 Photogrammetrie Fernerkundung Geoinformation [J]: 475-488. [https://doi.org/10.1127/1432-](https://doi.org/10.1127/1432-8364/2010/0069)
322 [8364/2010/0069](https://doi.org/10.1127/1432-8364/2010/0069)
- 323 Dao P D, Liou Y A 2015. Object-Based Flood Mapping and Affected Rice Field Estimation with Landsat
324 8 OLI and MODIS Data. Remote Sensing [J], 7: 5077-5097.
325 <https://doi.org/10.3390/rs70505077>
- 326 Diaz-Delgado R, Aragonés D, Afan I, et al. 2016. Long-Term Monitoring of the Flooding Regime and
327 Hydroperiod of Donana Marshes with Landsat Time Series (1974-2014). Remote Sensing [J],
328 8: 19. <https://doi.org/10.3390/rs8090775>
- 329 Fuentes I, Padarian J, Van Ogtrop F, et al. 2019. Spatiotemporal evaluation of inundated areas using
330 MODIS imagery at a catchment scale. Journal of Hydrology [J], 573: 952-963.
331 <https://doi.org/10.1016/j.jhydrol.2019.03.103>
- 332 Gao F, Masek J, Schwaller M, et al. 2006. On the blending of the Landsat and MODIS surface reflectance:
333 Predicting daily Landsat surface reflectance. Ieee Transactions on Geoscience and Remote
334 Sensing [J], 44: 2207-2218. <https://doi.org/10.1109/tgrs.2006.872081>
- 335 Gianinetto M, Villa P, Lechi G 2006. Postflood damage evaluation using landsat TM and ETM plus data
336 integrated with DEM. Ieee Transactions on Geoscience and Remote Sensing [J], 44: 236-243.
337 <https://doi.org/10.1109/tgrs.2005.859952>
- 338 Guo J Y, Luan Y J, Li Z, et al. 2021. Mozambique Flood (2019) Caused by Tropical Cyclone Idai
339 Monitored From Sentinel-1 and Sentinel-2 Images. Ieee Journal of Selected Topics in Applied
340 Earth Observations and Remote Sensing [J], 14: 8761-8772.
341 <https://doi.org/10.1109/jstars.2021.3107279>
- 342 Henry J B, Chastanet P, Fellah K, et al. 2006. Envisat multi-polarized ASAR data for flood mapping.
343 International Journal of Remote Sensing [J], 27: 1921-1929.
344 <https://doi.org/10.1080/01431160500486724>
- 345 Henry J B, Chastanet P, Fellah K, et al. ENVISAT multi-polarised ASAR data for flood mapping[C]//23rd
346 International Geoscience and Remote Sensing Symposium (IGARSS 2003). Toulouse,
347 France:Ieee,2003:1136-1138.
- 348 Hu Q, Zhu Y L, Hu H X, et al. 2021. Multiple Kernel Learning with Maximum Inundation Extent from
349 MODIS Imagery for Spatial Prediction of Flood Susceptibility. Water Resources Management
350 [J]: 19. <https://doi.org/10.1007/s11269-021-03010-2>
- 351 Khan S I, Hong Y, Wang J H, et al. 2011. Satellite Remote Sensing and Hydrologic Modeling for Flood

352 Inundation Mapping in Lake Victoria Basin: Implications for Hydrologic Prediction in
353 Ungauged Basins. *Ieee Transactions on Geoscience and Remote Sensing [J]*, 49: 85-95.
354 <https://doi.org/10.1109/tgrs.2010.2057513>

355 Liu H, Gong P, Wang J, et al. 2021. Production of global daily seamless data cubes and quantification of
356 global land cover change from 1985 to 2020-iMap World 1.0. *Remote Sensing of Environment*
357 *[J]*, 258: 23. <https://doi.org/10.1016/j.rse.2021.112364>

358 Liu W D, Baret F, Gu X F, et al. 2002. Relating soil surface moisture to reflectance. *Remote Sensing of*
359 *Environment [J]*, 81: 238-246.

360 Mallinis G, Gitas I Z, Giannakopoulos V, et al. 2013. An object-based approach for flood area delineation
361 in a transboundary area using ENVISAT ASAR and LANDSAT TM data. *International Journal*
362 *of Digital Earth [J]*, 6: 124-136. <https://doi.org/10.1080/17538947.2011.641601>

363 Mehrabi A 2021. Monitoring the Iran Pol-e-Dokhtar flood extent and detecting its induced ground
364 displacement using sentinel 1 imagery techniques. *Natural Hazards [J]*, 105: 2603-2617.
365 <https://doi.org/10.1007/s11069-020-04414-w>

366 Olthof I 2017. Mapping Seasonal Inundation Frequency (1985-2016) along the St-John River, New
367 Brunswick, Canada using the Landsat Archive. *Remote Sensing [J]*, 9: 16.
368 <https://doi.org/10.3390/rs9020143>

369 Pulvirenti L, Chini M, Pierdicca N, et al. 2011. Flood monitoring using multi-temporal COSMO-SkyMed
370 data: Image segmentation and signature interpretation. *Remote Sensing of Environment [J]*, 115:
371 990-1002. <https://doi.org/10.1016/j.rse.2010.12.002>

372 Sanyal J, Lu X X 2004. Application of remote sensing in flood management with special reference to
373 monsoon Asia: A review. *Natural Hazards [J]*, 33: 283-301.
374 <https://doi.org/10.1023/b:Nhaz.0000037035.65105.95>

375 Shen H F, Huang L W, Zhang L P, et al. 2016. Long-term and fine-scale satellite monitoring of the urban
376 heat island effect by the fusion of multi-temporal and multi-sensor remote sensed data: A 26-
377 year case study of the city of Wuhan in China. *Remote Sensing of Environment [J]*, 172: 109-
378 125. <https://doi.org/10.1016/j.rse.2015.11.005>

379 Shen Y, Zhang X Y, Wang W L, et al. 2021. Fusing Geostationary Satellite Observations with Harmonized
380 Landsat-8 and Sentinel-2 Time Series for Monitoring Field-Scale Land Surface Phenology.
381 *Remote Sensing [J]*, 13: 19. <https://doi.org/10.3390/rs13214465>

382 Tsyganskaya V, Martinis S, Marzahn P, et al. 2018. Detection of Temporary Flooded Vegetation Using
383 Sentinel-1 Time Series Data. *Remote Sensing [J]*, 10: 23. <https://doi.org/10.3390/rs10081286>

384 Voormansik K, Praks J, Antropov O, et al. 2014. Flood Mapping With TerraSAR-X in Forested Regions
385 in Estonia. *Ieee Journal of Selected Topics in Applied Earth Observations and Remote Sensing*
386 *[J]*, 7: 562-577. <https://doi.org/10.1109/jstars.2013.2283340>

387 Wang Q M, Tang Y J, Tong X H, et al. 2020. Virtual image pair-based spatio-temporal fusion. *Remote*
388 *Sensing of Environment [J]*, 249: 17. <https://doi.org/10.1016/j.rse.2020.112009>

389 Yan L, Roy D P 2018. Large-Area Gap Filling of Landsat Reflectance Time Series by Spectral-Angle-
390 Mapper Based Spatio-Temporal Similarity (SAMSTS). 10: 609.

391 Yan L, Roy D P 2020. Spatially and temporally complete Landsat reflectance time series modelling: The
392 fill-and-fit approach. *Remote Sensing of Environment [J]*, 241: 17.
393 <https://doi.org/10.1016/j.rse.2020.111718>

394 Zhang F, Zhu X L, Liu D S 2014. Blending MODIS and Landsat images for urban flood mapping.
395 *International Journal of Remote Sensing [J]*, 35: 3237-3253.

396 <https://doi.org/10.1080/01431161.2014.903351>
397 Zhang Q, Zhang P L, Hu X D 2021. Unsupervised GRNN flood mapping approach combined with
398 uncertainty analysis using bi-temporal Sentinel-2 MSI imageries. International Journal of
399 Digital Earth [J], 14: 1561-1581. <https://doi.org/10.1080/17538947.2021.1953160>
400 Zhu X L, Chen J, Gao F, et al. 2010. An enhanced spatial and temporal adaptive reflectance fusion model
401 for complex heterogeneous regions. Remote Sensing of Environment [J], 114: 2610-2623.
402 <https://doi.org/10.1016/j.rse.2010.05.032>
403 Zhu X L, Helmer E H, Gao F, et al. 2016. A flexible spatiotemporal method for fusing satellite images
404 with different resolutions. Remote Sensing of Environment [J], 172: 165-177.
405 <https://doi.org/10.1016/j.rse.2015.11.016>
406

407 **Authors and Affiliations**

408 **Zhicheng Wang^{1,2,3} Zhiqiang Gao^{2,3}**

409 Zhicheng Wang
410 zcwang@yic.ac.cn

411 Zhiqiang Gao
412 zqgao@yic.ac.cn

413 ¹ University of Chinese Academy of Sciences, Beijing 100049, PR China

414 ² CAS Key Laboratory of Coastal Environmental Processes and Ecological Remediation, Yantai
415 Institute of Coastal Zone Research, Chinese Academy of Sciences, Yantai Shandong 264003, P.R.
416 China

417 ³ Shandong Key Laboratory of Coastal Environmental Processes, Yantai Institute of Coastal Zone
418 Research, Chinese Academy of Sciences, Yantai Shandong 264003, P.R. China